RANS simulation of secondary flows in a low pressure turbine cascade: Influence of inlet boundary layer profile

Technopress, *Vol. 11, No. 1 (2016) 1–16*
DOI: http://dx.doi.org/2016.1111

Simulation of Secondary Flows in Turbomachinery by the Discontinuous Galerkin Method

Michele Errante*, Andrea Ferrero[a] and Francesco Larocca[b]

DIMEAS, Politecnico di Torino, Corso Duca degli Abruzzi 24, 10129 Torino, Italy

(Received -, Revised -, Accepted -)

Abstract. Secondary flows have a huge impact on the losses in low pressure gas turbines and the inlet boundary layer state is one of the factors which most affects the endwall flow field. The present work can be divided into two parts. The first one aims at investigating secondary flows in a low-pressure gas turbine cascade by means of RANS simulations for two different inlet conditions. The purpose of the second one is to estimate the influence of viscosity and turbulence on the end-wall flow field through a comparison between the RANS results and those obtained from an inviscid simulation with a prescribed inlet profile which mimics a boundary layer.. The equations are discretised in space by the Discontinuous Galerkin method and implicit time integration is adopted. Changes in the peculiarities of the flow field within the cascade passage are discussed. The results are compared with experimental and numerical data available in the literature.

Keywords: secondary flows; turbine cascade; boundary layer development; three-dimensional flow; CFD; discontinuous Galerkin

1. Introduction

Contrary to what might be deduced from the adjective “secondary”, the influence of secondary flows on the flow field in a gas turbine is an issue of paramount importance. In low-pressure turbines (LPTs) the set of complex three-dimensional vortex structures, originated from the interaction between the incoming end-wall boundary layer and the cascade, is responsible for a significant fraction of total losses.

Over the years, many authors have shed light on the nature of secondary flows. The review works carried out by Sieverding (1985) and Langston (2001) were crucial in summarizing the general flow topology of the vortex system generated by secondary flows. As discussed by Langston (1980), peculiar of that vortex system is the inlet boundary layer separation upstream of the leading edge due to the potential flow field induced by the blade, which provoke the formation of a horseshoe vortex (HP) with two legs stretching along the suction and pressure side of the blade. Due to the

*Corresponding author, Ph.D., E-mail: michele.errante@polito.it
[a]Assistant Professor, E-mail: andrea_ferrero@polito.it
[b]Professor, E-mail: francesco.larocca@polito.it

http://www.techno-press.org/?journal=sem&subpage=8 ISSN: 1225-4568(Print), 1598-6217(Online)

passage pressure-to-suction endwall flow (crossflow), the pressure-side leg of the horseshoe vortex is immediately moved away from the pressure side toward the suction side after it enters the passage, feeding the passage vortex (PV), with which it shares the same sense of rotation. The behavior of the other leg of the horseshoe vortex (suction side leg) has not been uniquely described. Sieverding and Van Den Bosche (1983) and Wang *et al.* (1997) observed that the suction leg wraps around the passage vortex through the passage. On the other hand, in the model proposed by Goldstein and Spores (1988) it moves upward on the suction surface. Furthermore, among the aerodynamic structures that constitute the secondary flows, the counter vortex (CV) has been reported in several studies, a vortex located above the passage vortex and counter-rotating with respect to it.

The current study has a twofold objective. Firstly, since it is known that one of the factors which most affects the end-wall flow field in a low pressure turbine cascade is the incoming boundary layer state (de la Blanco *et al.* 2003, Cui *et al.* 2017), this work aims to assess, by means of RANS analyses, how secondary flows change from the case of perfectly uniform inlet conditions to the case where a well defined boundary layer is present at the inlet of the T106 LPT linear cascade. Moreover, whereas the horseshoe vortex generation is an inviscid phenomenon, this study attempts to provide an estimation of the influence of viscosity and turbulence on the end-wall flow field through a comparison between the RANS results and those obtained from a further simulation performed by solving the Euler equations and imposing the same inlet velocity profile as in the RANS computation.

2. Test case description

The T106A cascade was selected for the investigations, a highly loaded low-pressure turbine cascade. It is characterised by a pitch t to axial chord c_x ratio of 0.929, a span H to axial chord c_x ratio of 2.206 and an inlet flow angle β_s equal to 37.7 deg with respect to the axial direction. Since the calculations are carried out using non-dimensional quantities, all geometric specifications are scaled with respect to the axial chord c_x. The Reynolds and Mach numbers were chosen according to the experimental study of Duden and Fottner (1997) and the numerical work of Pichler *et al.* (2019) and Marconcini *et al.* (2019), $Re = 120000$ and $M = 0.59$.

In Fig. 1 is shown the computational domain built for the RANS and Euler analysis, where x,y and z are the axial, spanwise and pitchwise directions, respectively. The leading edge is located at $x = 0$, the inlet is at $x = -0.8\ c_x$ and the outlet is at $x = 2\ c_x$, hence the total axial extension of the domain is set equal to 2.8 times the blade axial chord. Since the flow field is expected to be symmetrical with respect to the midspan plane, the spanwise extension of the domain is exactly equal to half of the span dimension, hence the end-wall surface is positioned at $y = 1.1029\ c_x$. While for Euler simulation inviscid wall boundary condition is imposed both at the midspan plane and end-wall, for RANS adiabatic boundary condition and inviscid wall boundary condition are imposed at the end-wall and midspan plane, respectively. In order to simulate a linear cascade, a periodic condition is used to connect the faces located at the pitchwise domain boundary.

As mentioned above, RANS computations were conducted for two different cases which differ in terms of inlet conditions. The first one, which will be referred to as C1, is obtained imposing uniform conditions on the inlet section. For the second case C2, an end-wall boundary layer profile reconstructed from the data available from Duden and Fottner (1997) and Pichler *et al.* (2019) was set on the inlet section. The same boundary layer profile employed in C2 was also used for the simulation

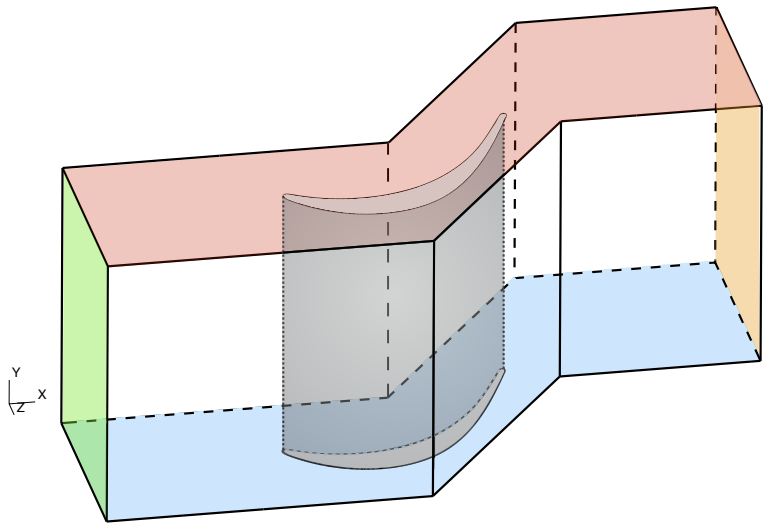

Fig. 1 Computational domain. The inlet and outlet planes are marked in green and orange respectively, while the midspan surface and the end-wall are colored blue and red, respectively.

Table 1 Inlet boundary layer parameters.

	C2 & Euler	Duden and Fottner (1997)
δ/c_x	0.3014	0.3005
δ^*/c_x	0.0452	0.0305
θ/c_x	0.0332	0.0332

in which the Euler equations were solved. The axial velocity u profile at the inlet is displayed in Fig. 2a and the values of boundary layer thickness δ, displacement thickness δ^* and momentum thickness θ referred to the axial chord c_x at inlet are shown in Table 1 together with the parameters of the experimental work conducted by Duden and Fottner (1997). In order to ensure the desired inlet boundary layer for C2 and Euler computations, the total pressure p° and total temperature T° shown in Fig. 2b, 2c were imposed as inlet boundary conditions. Furthermore, as will be mentioned below, since the Spalart-Allmaras (SA) turbulence model (Allmaras *et al.* 2012) is the closure model chosen for the RANS equations, for C2 is required to set the modified eddy viscosity (or Spalart Allmaras variable) $\tilde{\nu}$ as additional inlet boundary condition. The modified eddy viscosity $\tilde{\nu}$ profile multiplied by density ρ is illustrated in Fig. 2d.

3. Numerical Method

The simulations were performed by means of a research code which solves the unsteady, three-dimensional, Reynolds-averaged Navier-Stokes equations (for C1 and C2) and Euler equations in a finite elements framework, based on the Discontinuous Galerkin (DG) formulation. For RANS simulations, convective fluxes are discretized by means of an approximate Riemann problem solver implemented according to Pandolfi (1984), while for Euler simulation the local Lax-Friedrichs (Lax

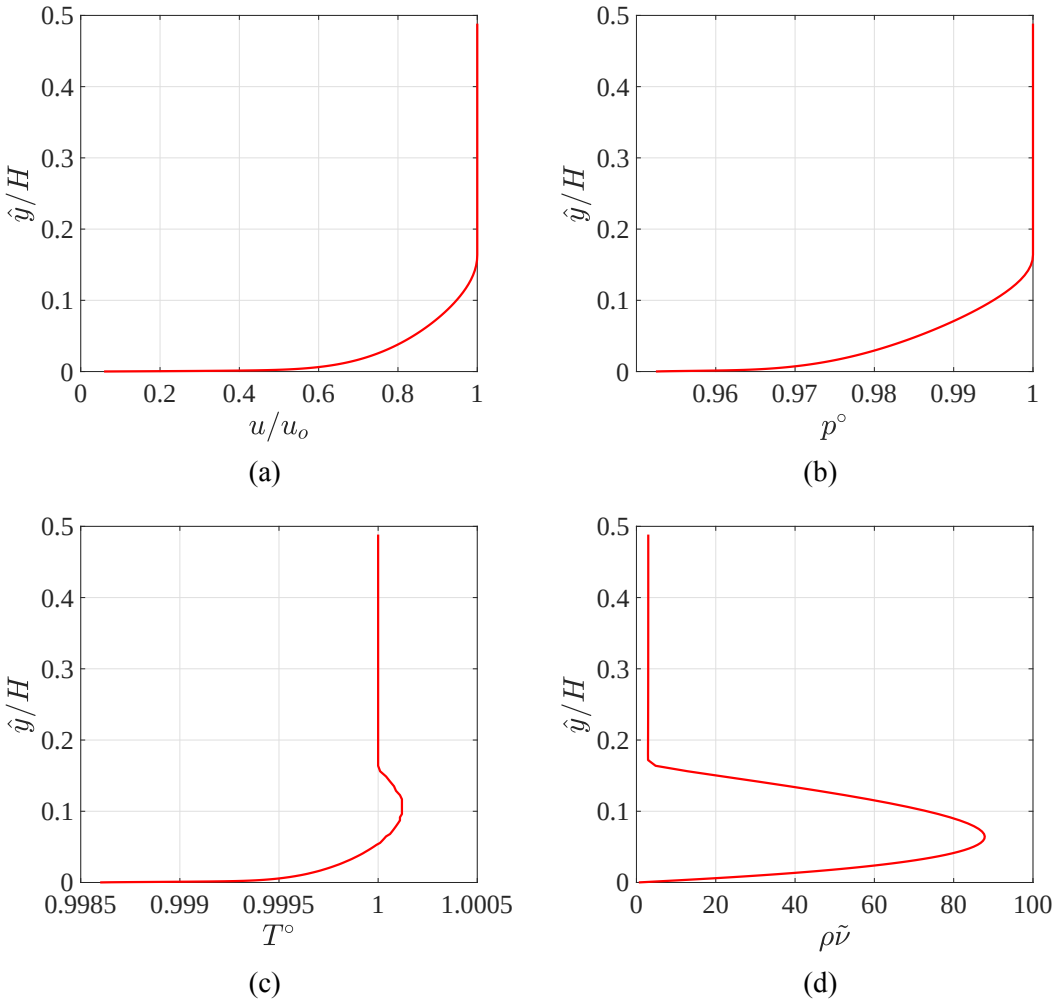

Fig. 2 Inlet spanwise distributions of (a) the axial component of velocity u, (b) total pressure p°, (c) total temperature T° and (d) modified eddy viscosity $\tilde{\nu}$, where $\hat{y}$ is the distance from the endwall, H is the span dimension, u_0 is axial velocity at the midspan plane and ρ is the density.

1954, Leveque 2002) or Rusanov (Rusanov 1962) flux is used. Moreover, for viscous computations the Enhanced Stability Recovery (ESR) approach proposed by Ferrero *et al.* (2015) is adopted for computing diffusive fluxes.

As already mentioned above, the closure model adopted for the RANS equations is the Spalart-Allmaras (SA) turbulence model, in the version described by Allmaras *et al.* (2012). The scheme selected for computations is second order accurate in space and for time discratization the implicit backward Euler scheme is used in order to get the steady solution by time-marching. The spatial domain is discretized, by the Gmsh tool of Geuzaine and Remacle (2009), using a multi-block grid assembled by an O-type structured grid around the blade profile and a non structured grid for the

remaining domain, for a total of about 2.4 million cells. Since a second order accurate DG scheme is used for RANS, there are 4 degrees of freedom in each cell and so the total number of degrees of freedom per equation for C1 and C2 is 9.6 million. Particular attention was paid to the size of elements close to the blade and in proximity of the end-wall, to ensure adequate spatial resolution for both the boundary layer and aerodynamic structures constituting the secondary flows.

4. Results

4.1 Streamlines

The most immediate way to visualize the aerodynamic structures that constitute the secondary flows is to observe the streamlines within the cascade passage. In Fig. 3 are shown the streamlines in the end-wall proximity, in particular those that at the inlet plane cover about 9% of the spanwise domain dimension, i.e. about 4% of the entire blade span length. In the images displayed the focus is on the exit of the cascade passage from which it is possible to notice how most of the vortex activity is relegated to the suction side, where it is clearly visible the passage vortex and the counter vortex. Making a comparison between C1 and C2, it is evident that the inlet boundary layer presence leads to a greater dimension of the secondary flows aerodynamic structures. Streamlines in C2, from about 9% of the spanwise domain dimension at inlet, reach more than 50% of the spanwise domain extent downstream of the trailing edge, in contrast to those in C1, which only reach just over 30%.

As mentioned above, since the origin of the horseshoe vortex does not depend on the presence of viscous effects, in Fig. 3c it is possible to see secondary flows streamlines obtained by solving Euler equations. Both pressure side and suction side legs appear more stretched in the pitchwise direction rather than the spanwise direction, occupying nearly 40% of the spanwise domain dimension downstream of the trailing edge.

4.2 Pressure distribution, C1 vs. C2

The evaluation of the pressure coefficient distribution c_p provides a very clear idea of the effects of secondary flows on the blade load variation along the span. It is defined as

$$c_p = \frac{p(x) - p_{out}}{p^{\circ}_{in} - p_{out}} \tag{1}$$

where p°_{in} is the freestream stagnation pressure at the inlet and p_{out} is the mass-average static pressure at the outlet.

With reference to Fig. 4, it can be seen that the presence of the inlet boundary layer for case C2 has a tangible influence close to the endwall, where the pressure and suction sides curves get closer,

Table 2 Evolution of lift coefficient C_L along the blade span, comparison between C1 and C2 results is shown.

C_L(C1)	C_L(C2)	$\hat{y}/H$	Var. (%)
0.752	0.613	0	-18.49
0.846	0.671	0.02	-20.72
0.878	0.852	0.15	-3.067
0.884	0.894	0.5	+1.122

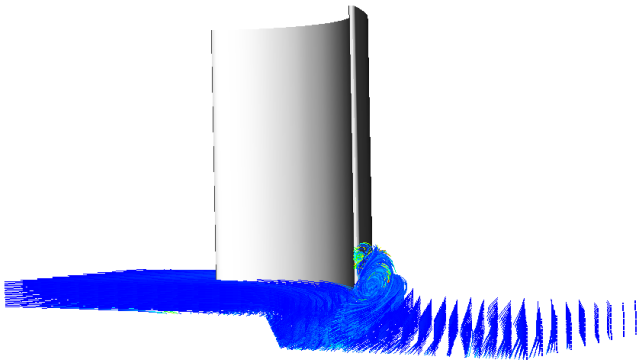

(a) C1

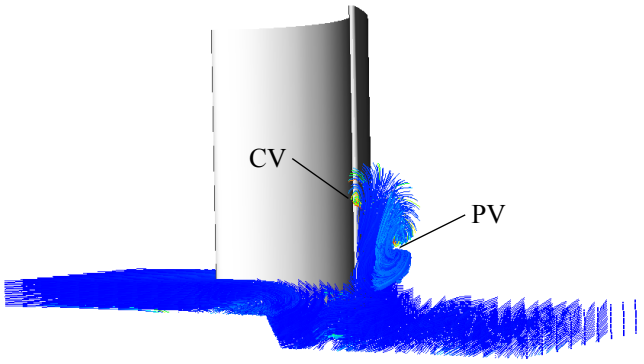

(b) C2

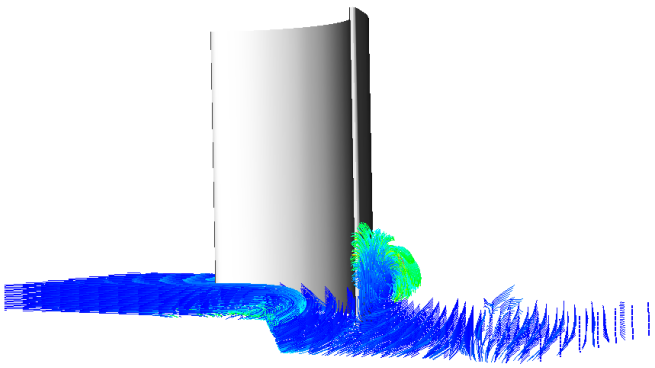

(c) Euler

Fig. 3 End-wall flow streamlines within the cascade passage. For C2, the passage vortex (PV) and the counter vortex (CV) are indicated.

narrowing the area between them. This is reflected in a reduction of lift generated by the blade as the endwall is approached from midspan passing from C1 to C2. What has just been said can also be

observed in Table 2 where the lift coefficient defined as:

$$C_L = \frac{L}{\frac{1}{2}\rho V_\infty^2 \left(c_x \cdot 1\right)} = \int_0^1 \left(c_{p_p} - c_{p_s}\right) d\left(\frac{x}{c_x}\right) \tag{2}$$

is evaluated at different spanwise locations $\hat{y}/H$ for C1 and C2, indeed for 0% and 2% of the span, the lift coefficient C_L falls by 20% moving from case 1 to case 2. Furthermore, referring to the results at $\hat{y}/H = 0$, it can be observed that the C2 curve follows the experimental results presented by Duden and Fottner (1997) very well, especially up to 80% of the profile axial chord.

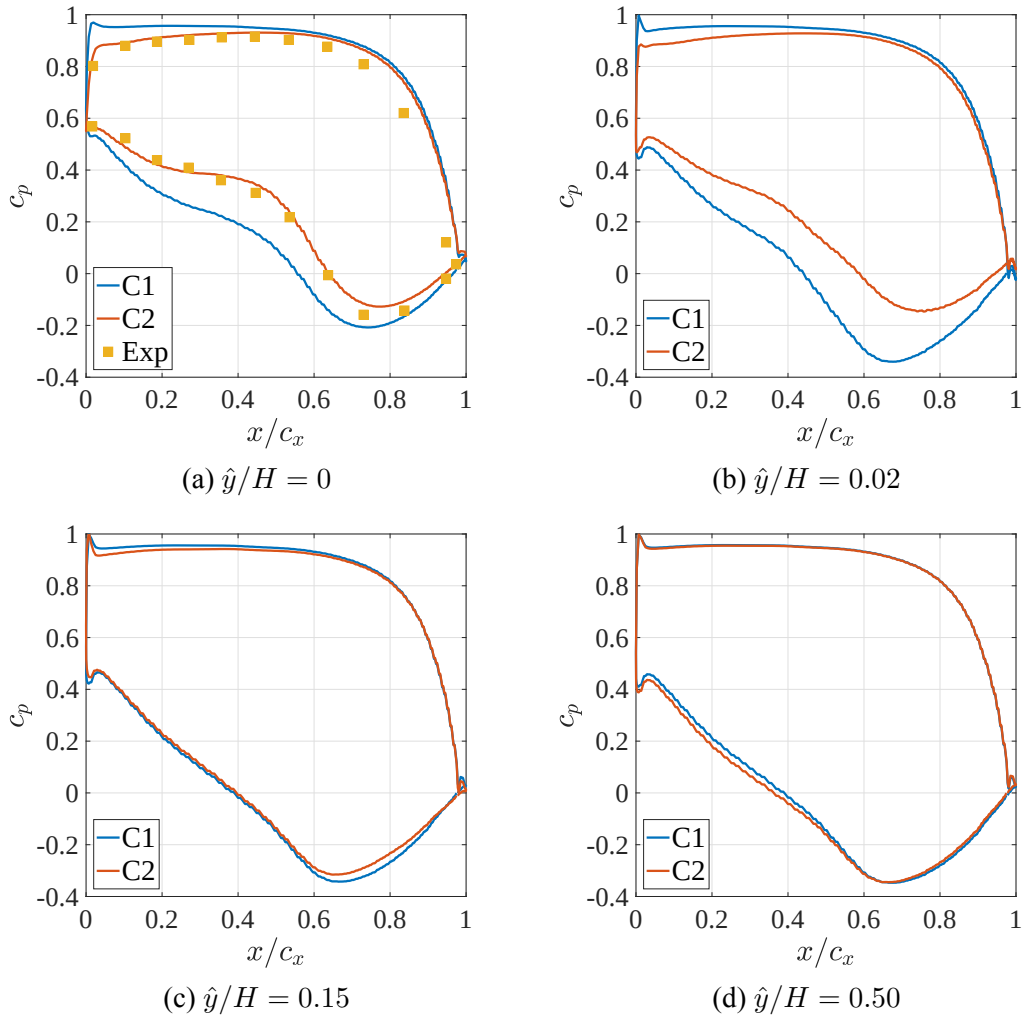

(a) $\hat{y}/H = 0$ (b) $\hat{y}/H = 0.02$

(c) $\hat{y}/H = 0.15$ (d) $\hat{y}/H = 0.50$

Fig. 4 Pressure distribution around the blade at different spanwise locations $\hat{y}/H$, where $\hat{y}$ is the distance from the endwall and H is the span dimension. The experimental data by Duden and Fottner (1997) labeled as "Exp" and presented with squares, are only available at $\hat{y}/H = 0$.

4.3 Flow angle evolution downstream of the blade trailing edge, C1 vs. C2

Figure 5 illustrates the mass-averaged flow angle β evolution downstream of the blade trailing edge. The distance from the endwall $\hat{y}$ divided by the span dimension H_1 used by Duden and Fottner (1997), approximately equal to 3.5 times the axial chord c_x, is reported on the ordinate axis, in order to make comparison with the experimental results possible. The peculiar pattern of a turbine cascade is visible: an overturning of the flow in proximity of the endwall followed by an underturning as the distance from the midspan decreases.

By comparing the two cases, it can be seen that both over turning and under turning phenomena are more pronounced and shifted towards the midspan in C2 than in C1. The difference between the two under turning peaks, distant from each other by $\Delta y/c_x = 0.15$ in the spanwise direction, is approximately equal to $\Delta\beta = 2.5°$, which corresponds to a relative increase of 4% passing from uniform conditions to a boundary layer profile at the inlet. On the other hand, the deviation between the two over turning maxima rises as x/c_x increases to an approximate value of $\Delta\beta = 7°$ for $x/c_x = 1.5$, corresponding to a relative increase of β of 10% by passing from C1 to C2. Furthermore, it can been observed that the data presented by Pichler *et al.* (2019) and Duden and Fottner (1997) follow the C2 curve pattern accurately. The differences between the numerical results are most likely due to the different turbulence models and possibly different boundary layer profiles.

4.4 Loss generation, C1 vs. C2

The spanwise distributions of the total pressure loss coefficient ω at different axial locations downstream the trailing edge defined as

$$\omega = \frac{p^{\circ}_{in} - p^{\circ}}{p^{\circ}_{in} - p}, \tag{3}$$

is shown in Fig 6, for which the calculations were performed by using a mass-averaging. It can be noticed that the two curves are very different from each other. The minimum value assumed by ω in C1 is always much smaller than that assumed in C2. Its percentage increase from the first case to the second one reaches values of around +300%. As far as the ω maximum is concerned, there is a trend reversal as the distance from the trailing edge grows: for $x/c_x = 1.03$ and $x/c_x = 1.10$ the maximum point in C1 is greater than in C2, whereas for $x/c_x = 1.30$ and $x/c_x = 1.50$ the ω positive peak in C2 becomes greater than in C1, with a percentage growth of about 15% for $x/c_x = 1.50$. Anyway, it is clear that the losses generated in C2 are averagely greater regarding those generated in C1 along the spanwise direction for all the axial locations. Regarding the comparison with the data available in the literature, as mentioned for the flow angle β, also for ω the experimental measurements by Duden and Fottner (1997) and the numerical results by Marconcini *et al.* (2019) match fairly well the C2 curve.

The losses generated by the secondary flows can be analyzed also by plotting the 2D loss coefficient contours at various axial locations (Fig. 7). The pattern of the distribution shows the so called "dog-bone" geometry, typical for highly loaded turbine cascades. For $x/c_x = 0.9$ it is possible to distinguish the vortices which produces more losses, such as the passage vortex, the corner vortex, the pressure side leg of the horseshoe vortex and the counter vortex, indicated by the labels PV, C, HP and CV, respectively. The two cases show a very similar overall pattern, however it can be seen that in C2 the losses are shifted towards the midspan plane and occupy a larger area in the pitchwise

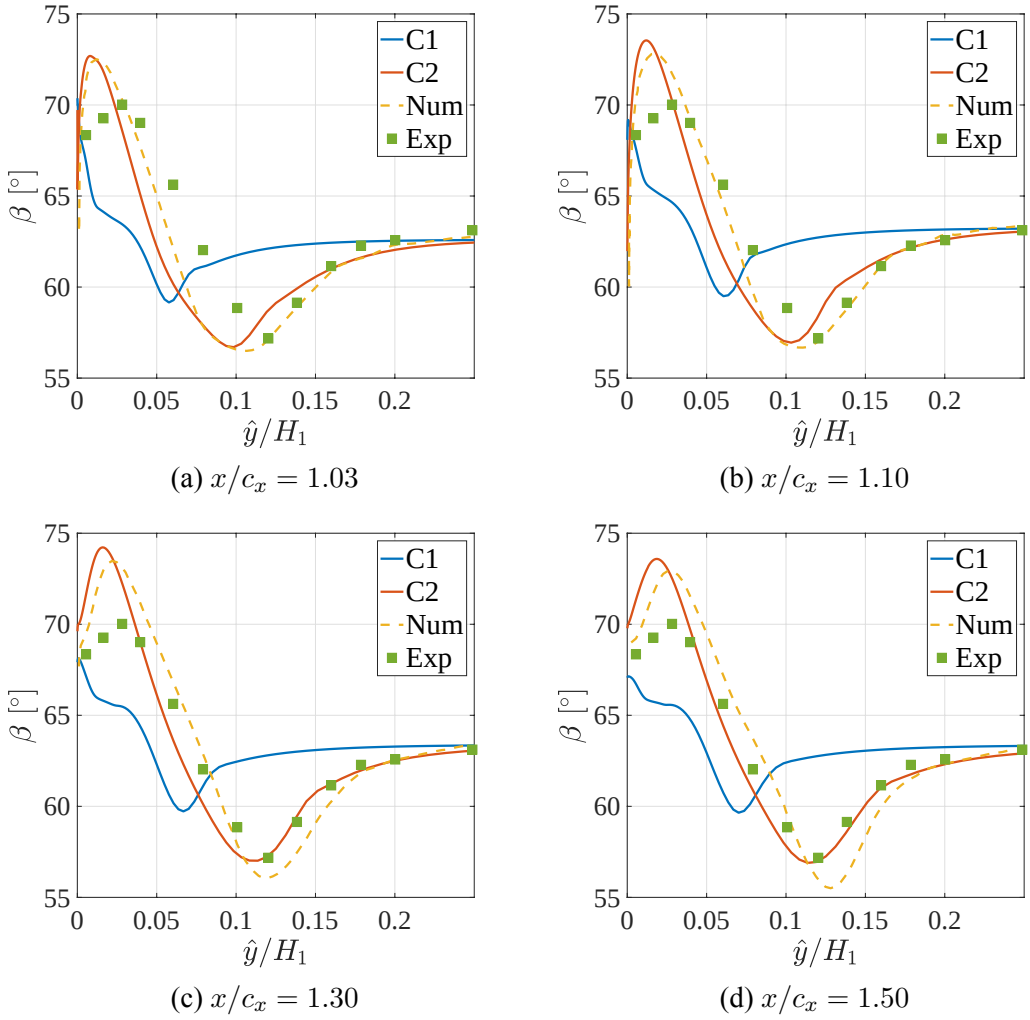

Fig. 5 Pitchwise averaged flow angle β with respect to the axial direction along the spanwise direction at four axial locations. The LES results by Pichler *et al.* (2019) labeled as "Num" are presented with dashed line and the Duden and Fottner (1997) experimental measurements labeled as "Exp", only available at $x/c_x = 1.50$, are presented with squares.

direction with respect to C1. In order to quantify this displacement, the distance between the passage vortex cores for C1 and C2 cases was measured, equal to $\Delta y/c_x = 0.12$. Additionally, at the axial locations $x/c_x = 1.10$, $x/c_x = 1.30$ e $x/c_x = 1.50$ the distance between point L and L', M and M', N and N' is equal to $\Delta y/c_x = 0.17$, $\Delta y/c_x = 0.20$, $\Delta y/c_x = 0.22$, respectively.

An analysis of Fig. 5, 6 and 7 reveals that for C2 the influence of secondary flows is present at further distances from the endwall than C1 in the spanwise direction. While the secondary flows effects for the former can be notice up to almost one axial chord c_x from the endwall, the effects of the latter can only be seen up to about half c_x.

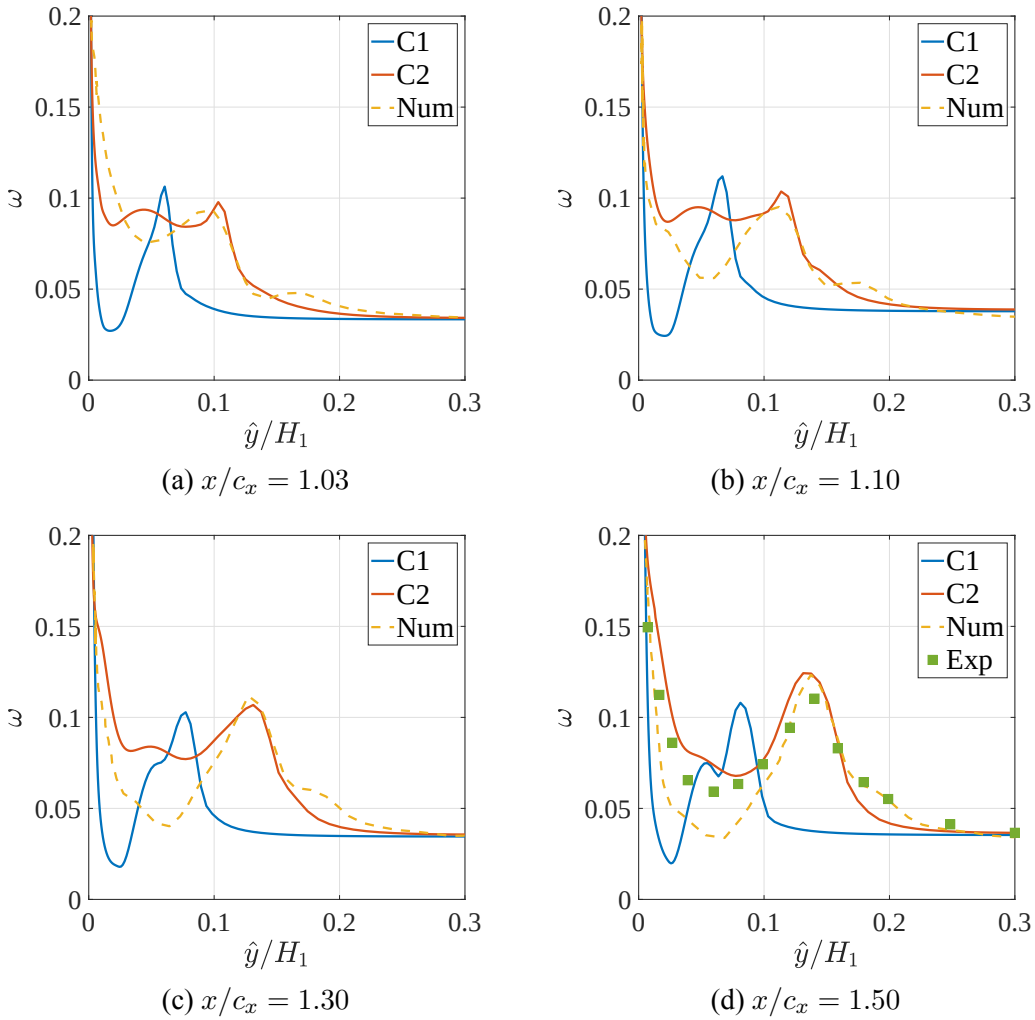

(a) $x/c_x = 1.03$ (b) $x/c_x = 1.10$

(c) $x/c_x = 1.30$ (d) $x/c_x = 1.50$

Fig. 6 Spanwise distributions of total pressure loss coefficient at four axial locations. The RANS results by Marconcini *et al.* (2019) labeled as "Num" are presented with dashed line and the Duden and Fottner (1997) experimental measurements labeled as "Exp", only available at $x/c_x = 1.50$, are presented with squares.

4.5 Euler vs. RANS - C2

The main purpose of this section is to identify differences in the Euler and RANS C2 predictions of secondary flows in order to estimate the influence of viscosity and turbulence on the end-wall flow field. As already mentioned, the horseshoe vortex generation is an inviscid phenomenon, as long as a flow velocity gradient is present near the end-wall. For this reason, the simulation that solves the Euler equations was conducted by imposing an inlet boundary layer. Without it, the flow would have been completely two-dimensional with velocity component in the spanwise direction equal to zero at every point of the domain.

With reference to Fig. 8, which shows the loss coefficient ω contours at different axial locations,

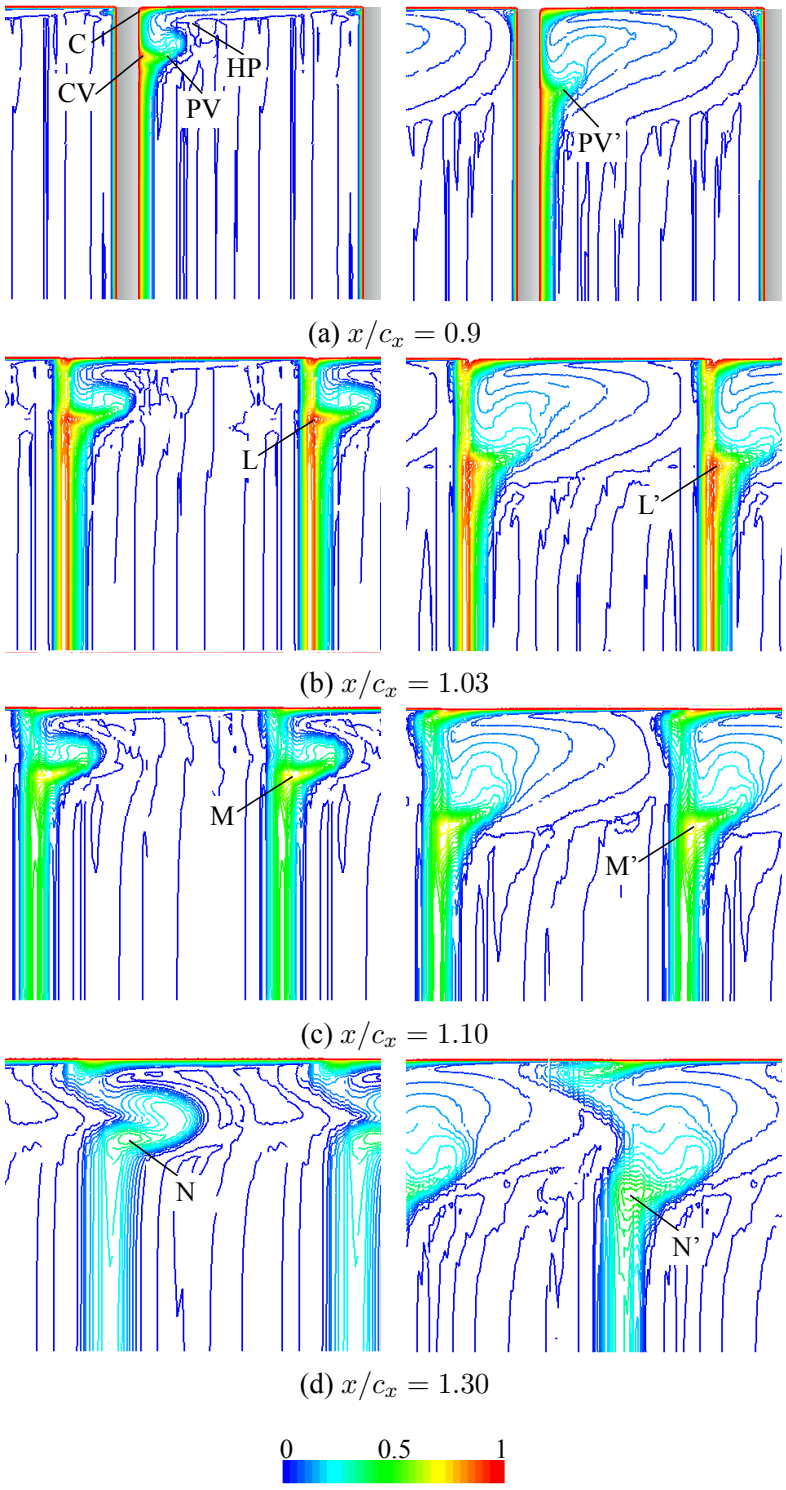

Fig. 7 Loss coefficient ω contours at four axial locations (left C1, right C2).

it can be appreciated that the losses estimated from Euler equations are well localized and confined to the only region of the domain where secondary flows vorticity dominates. In contrast to RANS, the cascade passage simulated solving Euler equations is mainly governed by a single large and homogeneous vortex structure, whose core does not move away from the end-wall proceeding downstream of the trailing edge.

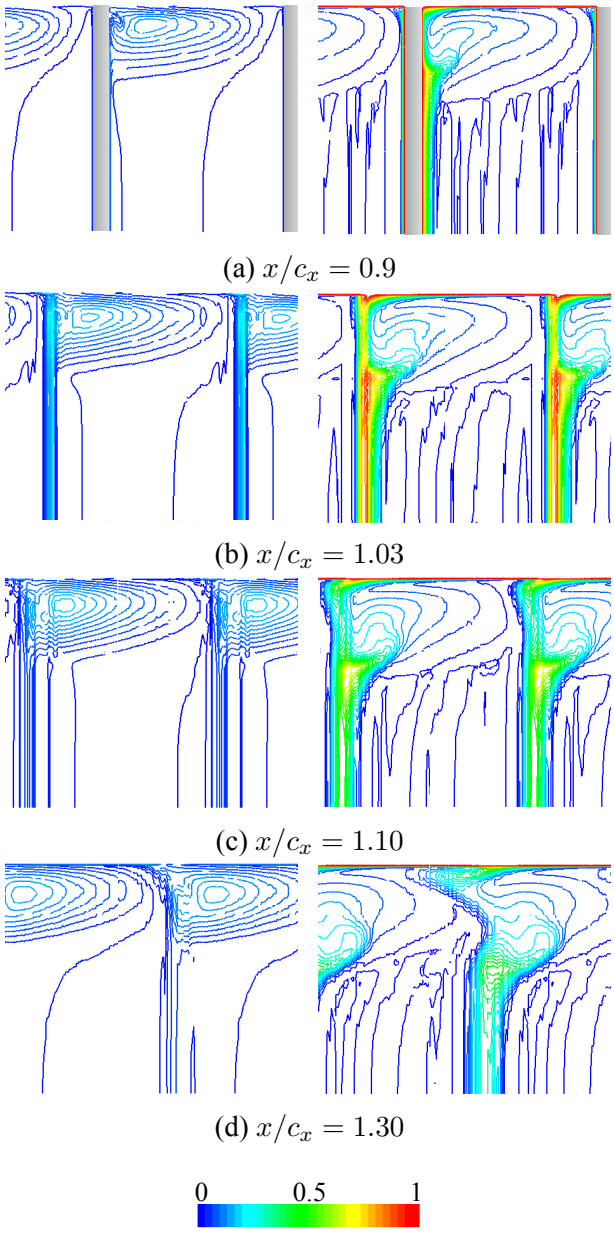

Fig. 8 Loss coefficient ω contours at four axial locations (left Euler, right C2).

Analyzing Fig. 9 illustrating the pitchwise averaged flow angle β along the spanwise direction for Euler and C2 cases, it is visible as the two average trends are not very distant from each other. The overturning angle is almost the same, although in the Euler case there is no a real overturning phenomena, since at $\hat{y}/H = 0$ the flow does not have zero velocity and is already oriented by an angle. On the contrary, the underturning peak is quite different: for C2 curve it is much greater and further from the end-wall than for Euler curve. Furthermore, the two distributions asymptotically reach the same value as expected, as away from the endwall and blade the compressible field tends to incompressible.

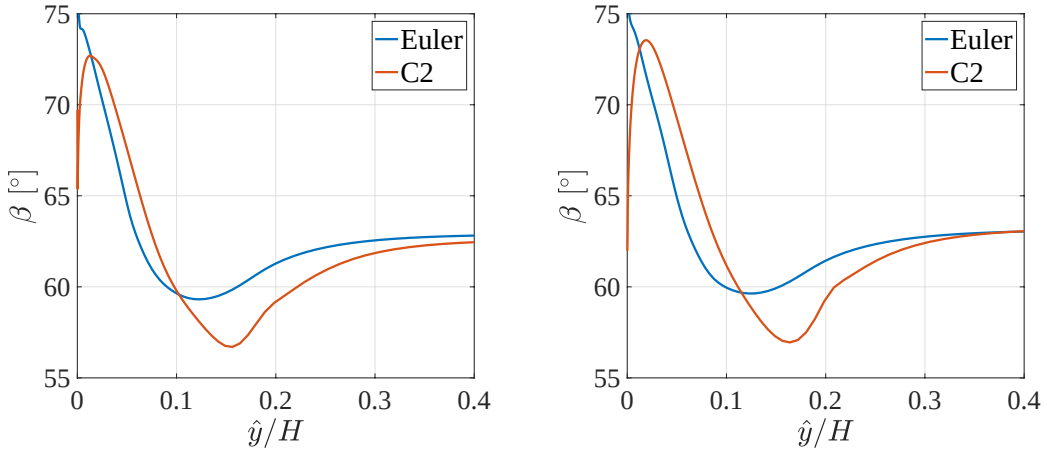

(a) $x/c_x = 1.03$ (b) $x/c_x = 1.10$

(c) $x/c_x = 1.30$ (d) $x/c_x = 1.50$

Fig. 9 Comparison of the pitchwise averaged flow angle β respect to the axial direction, obtained by solving Euler and RANS equations, along the spanwise direction at four axial locations.

Finally, in Fig. 10 is shown the pressure distribution around the blade at different spanwise locations $\hat{y}/H$, for RANS and Euler results. It is observed as the Euler curve is always under the C2

curve due to the absence of the boundary layer on the blade. However, at the end-wall ($\hat{y}/H = 0$), where the flow field is dominated by the effect of secondary flows vorticity, the two distributions are essentially overlapping.

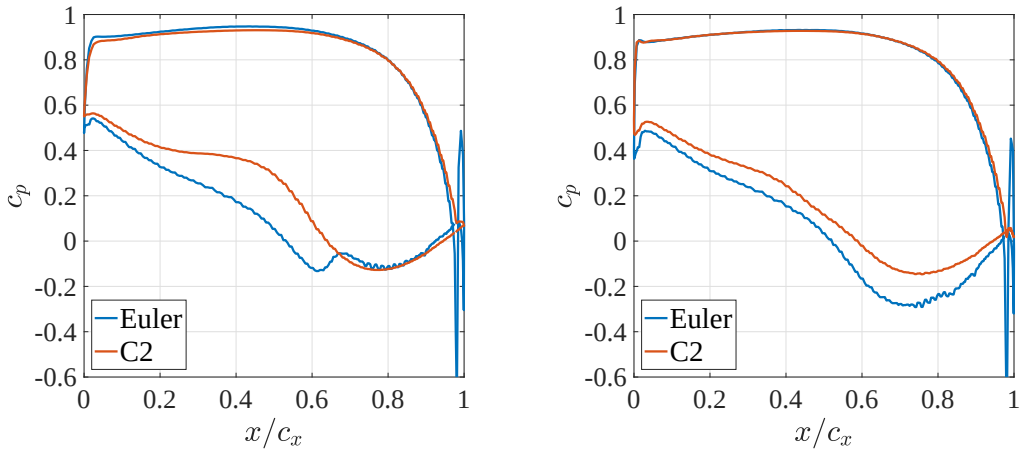

(a) $\hat{y}/H = 0$

(b) $\hat{y}/H = 0.02$

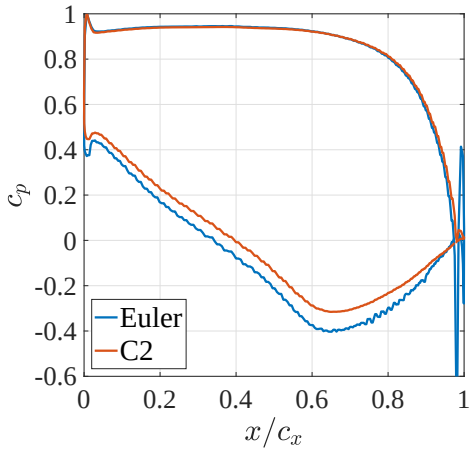

(c) $\hat{y}/H = 0.15$

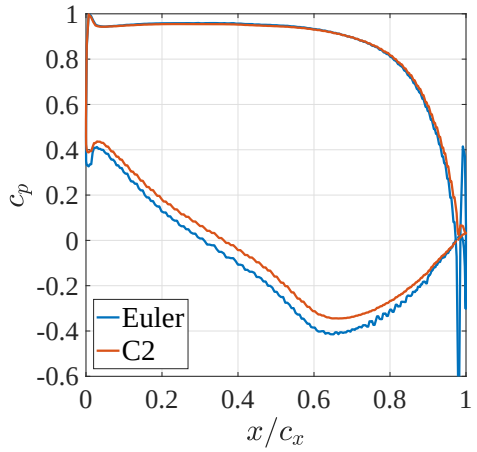

(d) $\hat{y}/H = 0.50$

Fig. 10 Pressure distribution around the blade at different spanwise locations $\hat{y}/H$. The results obtained by solving Euler and RANS equations are compared.

5. Conclusions

The flow field within the T106A linear cascade has been studied to examine the secondary flows details. This investigation aims at two main objectives. First of all two different inlet conditions have been inspected with RANS, inlet boundary layer and inlet uniform conditions, in order to explore the influence of incoming boundary layer over the end-wall flow. It has been observed that the presence

of an inlet boundary layer profile has a significant impact on the cascade flow field. Compared to the inlet uniform conditions case, the one with the inlet boundary layer has been found to be characterized by pronounced secondary flows structures. This can be seen in the evolution of streamlines along the passage, loss of lift close to the endwall, greater over turning and under turning angles, higher and more extended in space total pressure losses. In addition, it is noted that the influence of secondary flows is present up to a greater distance from the endwall due to the inlet boundary layer. Furthermore, comparisons with experimental (Duden and Fottner 1997) and numerical (Pichler *et al.* 2019, Marconcini *et al.* 2019) data available in the literature showed good agreement.

The second goal of the present work was to estimate the influence of viscosity and turbulence on the end-wall flow field. For this reason an additional simulation which solves the Euler equations was conducted by imposing the same inlet boundary layer used for the former RANS analysis. The results obtained are globally comparable, although they present evident differences. The cascade passage simulated with inviscid flow is mainly dominated by a single large and homogeneous vortex structure, less stretched in the spanwise direction and closer to the end-wall than the aerodynamic structures resulting from the compressible flow simulation.

Findings showed that for the chosen cascade with the Reynolds number and Mach number combination employed, a great part of the secondary flows details is strongly dependent on viscous phenomena. Therefore, the selection of the parameters with which to perform the RANS analysis and the choice of turbulence model are undoubtedly crucial to simulate the end-wall flow field for the present test-case. In this regard, it is emphasized that the comparisons made with the experimental and numerical data available in the literature have demonstrated that Spalart-Allmaras offers excellent results, considering that it is computationally cheaper than the model used by Pichler *et al.* (2019) and Marconcini *et al.* (2019).

Acknowledgements

Computational resources provided by hpc@polito, which is a project of Academic Computing within the Department of Control and Computer Engineering at the Politecnico di Torino (http://www.hpc.polito.it).

References

Sieverding, C. (1985), "Recent Progress in the Understanding of Basic Aspects of Secondary Flows in Turbine Blade Passages", *Journal of Engineering for Gas Turbines and Power*, **107**(2), 248–257.

Langston, L. (2001), "Secondary Flows in Axial Turbines—A Review", *Annals of the New York Academy of Sciences*, **934**(1), 11–26.

Langston, L. (1980), "Crossflows in a Turbine Cascade Passage", *Journal of Engineering for Power*, **102**(4), 866–874.

Sieverding, C., and Van Den Bosche, P. (1983), "The Use of Coloured Smoke to Visualize Secondary Flows in a Turbine-Blade Cascade", *Journal of Fluid Mechanics*, **134**, 85–89.

Wang, H., Olson, S., Goldstein, R., and Eckert, E. (1997), "Flow Visualization in a Linear Turbine Cascade of High Performance Turbine Blades", *Journal of Turbomachinery*, **119**(1), 1–8.

Goldstein, R., and Spores, R. (1988), "Turbulent Transport on the Endwall in the Region Between Adjacent Turbine Blades", *Journal of Heat Transfer*, **110**(4a), 862–869.

de la Blanco, E.R., Hodson, H., Vazquez, R., and Torre, D. (2003), "Influence of the state of the inlet endwall

boundary layer on the interaction between pressure surface separation and endwall flows", *Proceedings of the Institution of Mechanical Engineers, Part A: Journal of Power and Energy*, **217**(4), 433–441.

Cui, J., Rao, V. N., and Tucker, P. G. (2017), "Numerical Investigation of Secondary Flows in a High-Lift Low Pressure Turbine", *International Journal of Heat and Fluid Flow*, **63**, 149–157.

Duden, A. and Fottner, L. (1980), "Crossflows in a Turbine Cascade Passage", *Proceedings of the Institution of Mechanical Engineers, Part A: Journal of Power and Energy*, **211**(4), 309–320.

Pichler, R., Zhao, Y., Sandberg, R., Michelassi, V., Pacciani, R., Marconcini, M., and Arnone, A. (2019), "Large-Eddy Simulation and RANS Analysis of the End-Wall Flow in a Linear Low-Pressure Turbine Cascade, Part I: Flow and Secondary Vorticity Fields Under Varying Inlet Condition, *Journal of Turbomachinery*, **141**(12).

Marconcini, M., Pacciani, R., Arnone, A., Michelassi, V., Pichler, R., Zhao, Y., and Sandberg, R. (2019), "Large Eddy Simulation and RANS Analysis of the End-Wall Flow in a Linear Low-Pressure-Turbine Cascade—Part II: Loss Generation, *Journal of Turbomachinery*, **141**(5).

Allmaras, S., Johnson, F., and Spalart, P. (2012), *Seventh International Conference on Computational Fluid Dynamics (ICCFD7)*, Big Island, Hawaii.

Pandolfi, M. (1984), "A contribution to the numerical prediction of unsteady flows", *AIAA Journal*, **22**, 602–610.

Lax, P. D. (1954), "Weak solutions of nonlinear hyperbolic equations and their numerical computation", *Communications on Pure and Applied Mathematics*, **7**, 159–193.

Leveque, R.J. (2002), *Finite Volume Methods for Hyperbolic Problems*, Cambridge University Press.

Rusanov, V. V. (1985), "The calculation of the interaction of non-stationary shock waves and obstacles", *USSR Computational Mathematics and Mathematical Physics*, **1**(2), 304–320.

Ferrero, A., Larocca, F., and Puppo, G. (2015), "A robust and adaptive recovery-based discontinuous Galerkin method for the numerical solution of convection-diffusion equations", *International Journal for Numerical Methods in Fluids*, **77**(2), 63–91.

Geuzaine, C. and Remacle, J.-F. (2009), "Gmsh: a three-dimensional finite element mesh generator with built-in pre- and post-processing facilities.", *International Journal for Numerical Methods in Engineering*, **79**(11), 1309–1311.